Monthly Notices
of the
ROYAL ASTRONOMICAL SOCIETY

MNRAS **477,** 139–152 (2018) doi:10.1093/mnras/sty621

Morphological estimators on Sunyaev–Zel'dovich maps of MUSIC clusters of galaxies

Giammarco Cialone,[1★] Marco De Petris,[1★] Federico Sembolini,[1,2,3] Gustavo Yepes,[2,3★] Anna Silvia Baldi[1,4] and Elena Rasia[5]

[1]*Dipartimento di Fisica, Sapienza Università di Roma, p.le Aldo Moro 5, I-00185 Roma, Italy*
[2]*Departamento de Física Teórica, Módulo 8, Facultad de Ciencias, Universidad Autónoma de Madrid, E-28049 Cantoblanco, Madrid, Spain*
[3]*Astro-UAM, UAM, Unidad Asociada CSIC, E-28006, Madrid, Spain*
[4]*Dipartimento di Fisica, Università di Roma Tor Vergata, via della Ricerca Scientifica 1, I-00133 Roma, Italy*
[5]*INAF, Osservatorio Astronomico di Trieste, via Tiepolo 11, I-34131, Trieste, Italy*

Accepted 2018 March 5. Received 2018 March 5; in original form 2017 August 9

ABSTRACT

The determination of the morphology of galaxy clusters has important repercussions for cosmological and astrophysical studies of them. In this paper, we address the morphological characterization of synthetic maps of the Sunyaev–Zel'dovich (SZ) effect for a sample of 258 massive clusters ($M_{\rm vir} > 5 \times 10^{14}\,{\rm h}^{-1}\,{\rm M}_{\odot}$ at $z = 0$), extracted from the MUSIC hydrodynamical simulations. Specifically, we use five known morphological parameters (which are already used in X-ray) and two newly introduced ones, and we combine them in a single parameter. We analyse two sets of simulations obtained with different prescriptions of the gas physics (non-radiative and with cooling, star formation and stellar feedback) at four red shifts between 0.43 and 0.82. For each parameter, we test its stability and efficiency in discriminating the true cluster dynamical state, measured by theoretical indicators. The combined parameter is more efficient at discriminating between relaxed and disturbed clusters. This parameter had a mild correlation with the hydrostatic mass (∼0.3) and a strong correlation (∼0.8) with the offset between the SZ centroid and the cluster centre of mass. The latter quantity is, thus, the most accessible and efficient indicator of the dynamical state for SZ studies.

Key words: methods: numerical – galaxies: clusters: general – cosmology: theory.

1 INTRODUCTION

Clusters of galaxies are the largest virialized objects in the Universe and they play a key role in understanding the formation, the growth and the properties of large-scale structures. The investigation of cluster dynamical states has important astrophysical and cosmological implications. The disturbed nature of a cluster can be, in fact, an indicator of violent mergers. A sample of disturbed clusters would allow us to characterize the motion arising from these events. These events are of crucial importance for an accurate estimate of the non-thermal pressure support, which needs to be constrained to enable accurate determination of cluster cosmology (see e.g. Haiman, Mohr & Holder 2001; Borgani 2008; Mantz et al. 2010). As shown from numerical simulations, cluster masses derived from only the assumption of hydrostatic equilibrium, and thus accounting for only the contribution from thermal pressure, can be significantly underestimated (up to ∼30 per cent) (see e.g. Lau, Kravtsov & Nagai 2009; Rasia et al. 2012; Biffi et al. 2016, and references therein). This mass bias is reduced to 10 per cent in relaxed clusters. This is one of the main reasons for the common choice of calibrating the self-similar scaling relations (see e.g. Giodini et al. 2013, for a review) towards regular objects (see e.g. Johnston et al. 2007; George et al. 2012; Czakon et al. 2015).

Historically, the first attempts to determine whether a galaxy cluster was dynamically relaxed were made by visual inspections of the galaxy distribution in optical images (Conselice 2003) and the regularity of the intra-cluster medium (ICM) in X-ray maps (Ulmer & Cruddace 1982). A bimodal or clumpy surface brightness distribution was considered an indication of substructures in dynamically active clusters (Fabian 1992; Slezak, Durret & Gerbal 1994; Gómez et al. 1997; Rizza et al. 1998; Richstone, Loeb & Turner 1992), although some exceptions have been reported (e.g. Pinkney et al. 1996; Buote & Tsai 1996; Plionis 2002). On the other hand, the regular and mostly circular shapes of the projected gas distribution are characteristic of dynamically relaxed clusters, which have limited turbulent motion. From these early studies, several other morphological parameters have been introduced in the literature over the years (see Section 3.2), and more recent applications to X-ray maps can be found in Mantz et al. (2015), Nurgaliev et al. (2017), Andrade-Santos et al. (2017) and Lovisari et al. (2017).

No morphological evaluation has so far been drawn from Sunyaev–Zel'dovich (SZ) maps observed in the millimetric band.

★ E-mail: giammarcocialone@gmail.com (GC); marco.depetris@roma1.infn.it (MDP); gustavo.yepes@uam.es (GY)

The SZ effect (Sunyaev & Zeldovich 1970, 1972) is produced by the Comptonization of the cosmic microwave background (CMB) photons from the interaction with the energetic free electrons in the ICM and causes a redistribution of the energy of the CMB photons. This is observed as a variation on the CMB background whose intensity depends on the observed frequency. The CMB intensity variation is proportional to the integral of the electronic thermal pressure of the ICM along the line of sight (see e.g. Carlstrom, Holder & Reese 2002, for a review). Therefore, the SZ effect is linearly proportional to the electron number density. For this property, the SZ effect is a fundamental complementary tool to X-ray, since it probes the outermost regions of galaxy clusters more efficiently (see e.g. Roncarelli et al. 2013). Nowadays, hundreds or even thousands of galaxy clusters observed through the SZ effect are available thanks to different surveys carried out, either by ground-based facilities, like the South Pole Telescope (Chang et al. 2009; Staniszewski et al. 2009; Bleem et al. 2015) or the Atacama Cosmology Telescope (Swetz et al. 2011; Hasselfield et al. 2013), or space-based, like the *Planck* satellite (Planck Collaboration I 2011; Planck Collaboration XXIX 2014; Planck Collaboration XXVII 2016). Clusters detected through the SZ effect do not show significant bias in terms of relaxation state. For instance, Rossetti et al. (2016) showed that clusters detected by *Planck* – whose morphology is determined through the projected offset between the peak of the X-ray emission and the position of the brightest cluster galaxy (BCG) – are equally distributed between regular and disturbed objects. In contrast, in X-ray surveys the percentage of relaxed objects is ∼74 per cent. This comparison suggests that observational selection effects can seriously influence the result. Hence, it is important to evaluate morphology from SZ catalogues that are roughly mass-limited.

To infer cluster morphology from SZ maps, one would require high sensitivity and high angular resolution. At present, there are no SZ cluster catalogues with such characteristics. However, the situation might change in the coming years. Instruments like the currently operating MUSIC camera (Sayers et al. 2010) or MUSTANG-2 (Young et al. 2012), with maximum angular resolutions of ∼30 and ∼10 arcsec, respectively, are examples of microwave detectors aimed at producing high-resolution cluster imaging through the SZ effect. Very promising results have also been recently reported with the 30-m telescope at the IRAM observatory using the NIKA (Monfardini et al. 2010) and NIKA2 (Calvo et al. 2016; Adam et al. 2018) cameras. These maps reach an angular resolution of ∼20 arcsec (Adam et al. 2014; Mayet et al. 2017; Ruppin et al. 2017). Even better resolution has been achieved at low frequencies with interferometers, as shown in Kitayama et al. (2016). Indeed, they report the SZ imaging of a galaxy cluster at 5 arcsec from observations with the Atacama Large Millimeter Array (ALMA; Booth 2000). Since SZ maps correspond to the distribution of the thermal pressure, they are extremely valuable for the investigation of cluster morphology (see Wen & Han 2013; Cui et al. 2017, e.g.). For instance, Prokhorov et al. (2011) highlight the effects produced by a violent merger on the SZ imaging of a bullet-like simulated cluster, namely a cold substructure. Morphology has some impact also on the scaling relation between the integrated SZ signal and the cluster mass, as shown for simulated clusters (e.g. in da Silva et al. 2001; McCarthy et al. 2003; Shaw, Holder & Bode 2008). For instance, Rumsey et al. (2016) state that mergers induce small deviations from the canonical self-similar predictions in SZ and X-ray scaling relations, in agreement with Poole et al. (2007).

Apart from these examples, there is not yet a detailed study of the morphology derived from observed or simulated SZ maps, or of the relation between SZ morphology and cluster dynamical state. The aims of this paper are therefore: (1) to verify the feasibility of the application to SZ maps of morphological parameters typically used in X-ray, (2) to determine their effectiveness in segregating the cluster dynamical state (which for simulated clusters is known a priori) and (3) to evaluate their possible correlation with other relevant measures such as the hydrostatic mass bias or the X-ray morphological parameters. For these goals, we use both existing and new parameters and we also combine them to derive a global parameter.

The paper is organized as follows. In Section 2, we briefly describe the simulations and the data used in this analysis. In Section 3, we define the criteria used in the simulation to discriminate the dynamical state, and provide a summary of the morphological parameters. The efficiency and the stability of these parameters are tested in Section 4, which also compares their application to X-ray and SZ maps. Finally, the correlation of the morphological indicators with the hydrostatic mass bias and with the projected shift between the centre of mass (CM) and the centroid of the SZ map is investigated in Sections 5 and 6. We summarize our results and outline our conclusions in Section 7.

2 DATA SET

The analysis presented in this work is performed on simulated clusters taken from the MareNostrum-Multidark Simulations of Galaxy Clusters (MUSIC)[1] (Sembolini et al. 2013). The MUSIC project has two distinct subsets of re-simulated galaxy groups and clusters: MUSIC-1, which is built with objects extracted from the MareNostrum simulation (Gottlöber & Yepes 2007), and MUSIC-2, which is built with systems selected from the multidark simulations (Prada et al. 2012). The resimulations of all clusters are based on the initial conditions generated by the zooming technique of Klypin et al. (2001) and cover a spherical region centred on the red-shift-zero cluster with a radius of $6\,h^{-1}$ Mpc. The Lagrangian regions are resimulated with the inclusion of the baryonic physics and at higher resolution. The re-simulations are carried out using the TREEPM+SPH GADGET-2 code and include two different prescriptions for the gas physics. The simplest follows the evolution of a non-radiative gas, while the other includes several physical processes, such as cooling, UV photoionization, stellar formation, and thermal and kinetic feedback processes associated with supernovae explosions (for details, see Sembolini et al. 2013). We will refer to them as the NR and the CSF subsets, respectively. The final resolution is $m_{\rm DM} = 9 \times 10^8\,h^{-1}\,M_\odot$ for the dark matter (DM) and $m_{\rm gas} = 1.9 \times 10^8\,h^{-1}\,M_\odot$ for the initial gas elements.

In this work, we use a sample of 258 massive clusters, having virial mass $M_{\rm vir} > 5 \times 10^{14}\,h^{-1}\,M_\odot$ at $z = 0$, extracted from the MUSIC-2 data set. We analyse clusters simulated with both ICM versions, and considered at four different times of their cosmic evolution, namely at red shifts $z = 0.43, 0.54, 0.67$ and 0.82. The underlying cosmological model is that of the multidark parent simulation and it adopts the best-fitting parameters from *WMAP7*+BAO+SNI: $\Omega_{\rm m} = 0.27$, $\Omega_b = 0.0469$, $\Omega_\Lambda = 0.73$, $\sigma_8 = 0.82$, $n = 0.95$ and $h = 0.7$ (see Komatsu et al. 2011). This sample has been extensively analysed, with a focus on the baryon and SZ properties (Sembolini et al. 2013), on the X-ray scaling relations (Biffi et al. 2014) and on the motions of both DM and gas (Baldi et al. 2017).

[1] http://music.ft.uam.es

2.1 Sunyaev–Zel'dovich maps and X-ray data

The SZ effect can be separated into two components: the thermal component, produced by the random motion of the electrons in the ICM, and the kinetic component, generated by the overall bulk motion of the cluster with respect to the CMB rest frame (see e.g. Carlstrom et al. 2002). In this work, we focus only on the former. This produces a shift of the CMB brightness $I_{\rm CMB}$:

$$\frac{\Delta I}{I_{\rm CMB}} = \frac{x^4 {\rm e}^x}{({\rm e}^x - 1)^2} \left[x \coth\left(\frac{x}{2}\right) - 4 \right] y, \quad (1)$$

where $x = h_{\rm P}\nu/(k_{\rm B}T_{\rm CMB})$. ν is the frequency of the radiation, $h_{\rm P}$ is the Planck constant, $k_{\rm B}$ is the Boltzmann constant and $T_{\rm CMB}$ is the CMB temperature. The y factor in equation (1) is the Compton parameter, defined as

$$y = \frac{\sigma_{\rm T} k_{\rm B}}{m_{\rm e} c^2} \int n_{\rm e} T_{\rm e} \, {\rm d}\ell, \quad (2)$$

where $\sigma_{\rm T}$ is the Thomson cross-section, $m_{\rm e}c^2$ is the electron rest mass, $n_{\rm e}$ is the electron number density, $T_{\rm e}$ is the electron temperature and the integration is performed over the line of sight. To produce maps of the Compton parameter of our simulated clusters, we refer to the discretized version of the formula proposed in Flores-Cacho et al. (2009):

$$y \simeq \frac{\sigma_{\rm T} k_{\rm B}}{m_{\rm e} c^2} \sum_i W_{\rm p}\left(|\boldsymbol{r}_i - \boldsymbol{r}_{\rm cm}|, h_{\rm s}\right) n_{{\rm e},i} T_{{\rm e},i} \Delta\ell, \quad (3)$$

where the $W_{\rm P}$ function is the projected normalized spherical spline kernel of the simulation, i.e. the kernel presented in Monaghan & Lattanzio (1985). The kernel depends on the Smoothed Particle Hydrodynamics smoothing length $h_{\rm s}$ and is evaluated at the radial distance of the ith particle with respect to the cluster CM, $|\boldsymbol{r}_i - \boldsymbol{r}_{\rm cm}|$. The sum in equation (3) extends to all gas particles located along the line of sight up to a maximum distance $1.5R_{\rm vir}$ from the cluster centre, with $R_{\rm vir}$ the virial radius.

The side of the maps has a physical size of 10 Mpc, corresponding to ∼3.4 times the mean virial radius of the sample. This extension is comparable with the maximum radius that can be probed with SZ measurements of large clusters, which e.g. for *Planck* is of the order of a few virial radii (Planck Collaboration V 2013). Each pixel is equivalent to 10 kpc. In angular distances, given the cosmological parameters adopted in the simulation, the field of view and the pixel resolution correspond to (29.6, 26.1, 23.6, 21.8) arcmin and (1.8, 1.6, 1.4, 1.3) arcsec at the four red shifts ($z = 0.43, 0.54, 0.67, 0.82$), respectively. Such large fields of view could be covered with large mosaics of detectors and multiple observational runs. For example, one would need four to nine pointings with the MUSIC camera, which has a field of view of ∼10 arcmin. The angular resolution of our maps, instead, is not achievable by any current instrument, which at best reaches 5 arcsec for interferometric measurements (e.g. with ALMA), and about 20 arcsec for single-dish measurements (e.g. with the NIKA2 camera). In Section 4.4, we will degenerate the SZ signal to reproduce the angular resolution of three examples of existing telescopes for microwave astronomy, having diameters of 1.5, 10 and 30 m, respectively.

In this work, we do not consider specific observational features, such as instrumental noise or any contamination with astrophysical origins. These will be properly taken into account in a forthcoming work, which will address the capabilities of a specific experiment. The noise, indeed, typically shows a significant pixel-to-pixel correlation, and it is an intrinsic characteristic of the instrument. Astrophysical sources of contamination also depend on the instrument, in particular on the observed frequencies. In this study, we refer to noiseless and maps without any contamination, to be as general as possible.

In Section 4.1.1, we compare the morphological parameters derived from SZ with those obtained from X-ray data. We use two sub-samples of the non-radiative clusters selected in Meneghetti et al. (2014) to match morphologically the CLASH sample observed by *Chandra* and *XMM–Newton* in X-ray (Postman et al. 2012). These sub-samples have 79 clusters at $z = 0.43$ and 86 clusters at $z = 0.67$. Their X-ray maps were produced using the X-MAS software package (see Gardini et al. 2004; Rasia et al. 2008) to mimic ACIS-S3 *Chandra* observations, with a field of view of 8.3 arcmin and angular resolution of 0.5 arcsec.

3 DETERMINATION OF THE DYNAMICAL STATE

Before presenting the morphological parameters, we introduce the indicators of the cluster dynamical state that, in simulations, can be measured quantitatively from several estimators. For instance, one of the most used indicators in the literature is the ratio between the kinetic energy T and the potential energy W of the system measured within the virial radius. The ratio is expressed as $(2T - E_{\rm S})/|W|$, where $E_{\rm S}$ is the surface pressure energy evaluated at the same virial radius. A cluster is considered relaxed when the ratio is less than 1.35 (see e.g. Neto et al. 2007; Ludlow et al. 2012). Even if broadly adopted, in this paper we prefer to avoid it, since several works have shown that it is often unreliable (see e.g. Sembolini et al. 2014; Klypin et al. 2016). Another criterion is based on the ratio of the gas velocity dispersion σ over the theoretical velocity dispersion $\sigma_{\rm t}$ (Cui et al. 2017). This indicator, often expressed as $\zeta = \sigma/\sigma_{\rm t}$, can be applied to optical data, but it is still not clear whether the threshold that discriminates between relaxed and disturbed objects is dependent on mass.

3.1 Indicators of the dynamical state

In this work, the cluster dynamical state is quantified through the following two parameters, derived from 3D information of the simulated cluster. For this reason, we also call them 3D indicators:

(i) The ratio between the mass of the biggest substructure and the cluster mass evaluated within the virial radius: $M_{\rm sub}/M_{\rm vir}$. Some variants of this parameter exist, including the ratio between the mass of all substructures and the total cluster mass (see e.g. Meneghetti et al. 2014; Biffi et al. 2016). However, we use the simplest definition, as e.g. in Sembolini et al. (2014).

(ii) The offset Δ_r between the position of the peak of the density distribution $\mathbf{r}_\delta$ and the position of the CM of the cluster $\mathbf{r}_{\rm cm}$, normalized to the virial radius $R_{\rm vir}$:

$$\Delta_r = \frac{|\mathbf{r}_\delta - \mathbf{r}_{\rm cm}|}{R_{\rm vir}}. \quad (4)$$

We classify a cluster as relaxed if both indicators are simultaneously smaller than a certain threshold, which we fix to 0.1 in both cases. In the literature, different thresholds are adopted for DM-only simulations (see e.g. Macciò et al. 2007; D'Onghia & Navarro 2007). In particular, for the offset parameter, often a smaller value is used for the threshold. However, we prefer to increase it to 0.1 to accommodate the effect of baryons, which reduce the displacement due to their collisional nature. The fraction of relaxed

Table 1. Percentages of clusters classified as relaxed or disturbed for the four red shifts considered and the two ICM physics.

	CSF		NR	
z	Relaxed per cent	Disturbed per cent	Relaxed per cent	Disturbed per cent
0.43	56	44	55	45
0.54	53	47	53	47
0.67	56	44	55	45
0.82	54	46	53	47

and disturbed clusters is shown in Table 1, for all the analysed data sets. No significant dependence on red shift or ICM physics is seen in our data. Our sample has about 55 per cent of relaxed objects.

3.2 Morphological parameters

In the following, we describe the morphological parameters analysed in this work: the *asymmetry parameter*, the *fluctuation parameter*, the *light concentration parameter*, the *third-order power ratio parameter*, the *centroid shift parameter*, the *strip parameter*, the *Gaussian fit parameter* and a *combined parameter*. The first five indicators are taken from X-ray morphological studies, while we introduce here the remaining parameters. Here, we will discuss their expected behaviour for relaxed and disturbed clusters.

All the parameters refer to the centroid of the analysed SZ map as the centre and we computed them inside different values of the *aperture radius* $R_{\rm ap}$, equivalent to 0.25, 0.50, 0.75 and 1.00 times $R_{\rm vir}$. We will discuss which aperture works best for each parameter (see Section 4).

3.2.1 *Asymmetry parameter,* A_θ

This parameter, originally introduced by Schade et al. (1995), is based on the normalized difference between the original SZ map I and the rotated map R_θ, where θ is the rotation angle:

$$A_\theta = \frac{\sum\limits_{r<R_{\rm ap}} |I - R_\theta|}{\sum\limits_{r<R_{\rm ap}} I}, \tag{5}$$

where the sums are extended to all pixels within $R_{\rm ap}$. We computed four different versions of this parameter: A_x, A_y, A_π and $A_{\pi/2}$. For A_x and A_y, we consider R_θ to be the flipped image along the x- or y-axes, respectively (as in Rasia, Meneghetti & Ettori 2013). Low values of A_θ indicate relaxed clusters. We use the rotation angle corresponding to the maximum value of A_θ for the final classification.

3.2.2 *Fluctuation parameter,* F

The fluctuation parameter, introduced in Conselice (2003), is defined like the asymmetry parameter. Namely, it is expressed as the normalized difference between an original image I and its Gaussian-smoothed version B:

$$F = \frac{\sum\limits_{r<R_{\rm ap}} |I - B|}{\sum\limits_{r<R_{\rm ap}} I}. \tag{6}$$

Various versions of this parameter exist. Negative residuals are ignored in Conselice (2003), absolute values are not considered in Okabe et al. (2010) or different values for the full-width at half-maximum (FWHM) Gaussian filter are used. We keep the absolute values to account for both negative and positive residuals. Furthermore, we consider 10 equally spaced FWHM values, from $0.05R_{\rm vir}$ to $0.5R_{\rm vir}$, to evaluate the most effective choice. Regular clusters are expected to have low values of the fluctuation parameter.

3.2.3 *Light concentration parameter,* c

This parameter was introduced by Santos et al. (2008) to segregate cool core and non-cool core clusters (see also Cassano et al. 2010; Rasia et al. 2013). These analyses, based on X-ray maps, reach at best R_{500} (and only in a few cases do they go beyond).[2] Here we use a more general mathematical formula given by the ratio of the surface brightness computed within a radius r_2 and the one evaluated within a more central region of radius $r_1 < r_2$:

$$c = \frac{\int_0^{r_1} S(r)\,{\rm d}r}{\int_0^{r_2} S(r)\,{\rm d}r}. \tag{7}$$

We choose the inner and outer radii as fractions of the virial radius to avoid any dependence on the red shift when assuming a fixed physical aperture (as discussed in Hallman & Jeltema 2011) as was done in Santos et al. (2008). In particular, we set $r_2 = R_{\rm ap}$, and we use 10 different values of r_1, uniformly sampled between 0.1 and 1.0 times r_2. We expect higher values of c for relaxed clusters, since in this case the surface brightness peaks near the cluster centre, and lower values for disturbed ones, due to their irregular shape and the possible presence of structures far from the centre.

3.2.4 *Third-order power ratio parameter,* P_3/P_0

The first definition of the mth-order power ratio $P_{\rm m}/P_0$ was given by Buote & Tsai (1995):

$$\frac{P_{\rm m}}{P_0} = \frac{a_{\rm m}^2 + b_{\rm m}^2}{2m^2 R_{\rm ap}^2 a_0 \ln(R_{\rm ap})}, \tag{8}$$

where the coefficients $a_{\rm m}$ and $b_{\rm m}$ are, respectively, defined as:

$$a_{\rm m}(R_{\rm ap}) = \int\limits_{r\le R_{\rm ap}} S(r,\phi) r^m \cos(m\phi)\,{\rm d}r\,{\rm d}\phi, \tag{9}$$

$$b_{\rm m}(R_{\rm ap}) = \int\limits_{r\le R_{\rm ap}} S(r,\phi) r^m \sin(m\phi)\,{\rm d}r\,{\rm d}\phi, \tag{10}$$

and $S(r, \phi)$ is the surface brightness expressed as a function of the projected radius and azimuthal angle ϕ. Following this definition, we compute the third-order power ratio P_3/P_0 considering $m = 3$, and we take its decimal logarithm. This parameter is one of the most efficient in X-ray (see e.g. Rasia et al. 2013; Lovisari et al. 2017). We measure P_3/P_0 using four different aperture radii, expressed as fractions of the virial radius, and then consider its maximum value to better identify clusters with substructures or an irregular shape, which are associated with high values of the power ratio.

3.2.5 *Centroid shift parameter,* w

The centroid shift parameter is a measure of how much the centroid of a map with different circular sub-apertures changes. Once the centroid within $R_{\rm ap}$ is computed, a new aperture radius is defined

[2] R_{500} is the radius of a spherical volume enclosing a density 500 times larger than the critical density.

and the respective centroid is found. The operation is repeated for N sub-apertures. The centroid shift is then defined as the normalized standard deviation of all Δ_i separations:

$$w = \frac{1}{R_{\rm ap}} \sqrt{\frac{\sum(\Delta_i - \langle\Delta_i\rangle)^2}{N-1}}, \tag{11}$$

where $\langle\Delta_i\rangle$ is their mean value. This parameter has been widely applied on X-ray maps in several works, although some variations in its definition have been considered. Generally, it has been found to be an efficient parameter for discriminating a cluster's dynamical state (see e.g. Mohr et al. 1993; O'Hara et al. 2006; Poole et al. 2006; Maughan et al. 2008; Ventimiglia et al. 2008; Jeltema et al. 2008; Böhringer et al. 2010; Weißmann et al. 2013). A substructure will increase the value of the centroid shift; therefore, we expect low values for relaxed clusters. However, this might not be the case for symmetric substructures, which may not be identified using w.

3.2.6 *Strip parameter,* S

A strip is a profile extracted from the SZ map that passes through its centroid. The strip parameter is the sum of the pixel-to-pixel difference between couples of different strips, S_i and S_j, at N total different angles in absolute value. To obtain S between 0 and 1, this sum is normalized by the maximum strip integral and by the number of strip pairs considered:

$$S = \frac{\sum_{j,j<i} |S_i(r) - S_j(r)|}{(N(N-1)/2)\max\left[\int_{R_{\rm ap}} S_i(r)\,{\rm d}r\right]}. \tag{12}$$

As usual, $R_{\rm ap}$ indicates the aperture radius, i.e. the maximum radius within which the integration of the strips is performed. The main advantage of using this parameter is the possibility of using many non-repeated combinations of strips. Indeed, in this way the parameter quantifies the different contributions to the overall symmetry of the cluster SZ map from multiple angles. In our case, performing a single rotation of the SZ maps, we take four strips selected with angles equal to 0°, 45°, 90° and 135°, for a total of six computed differences. We have tested the effects of using $N > 4$ angles, finding that the dynamic range of this parameter is slightly reduced with an increasing number of strips. Nevertheless, the overlap between the populations of relaxed and disturbed objects remains substantially unchanged, allowing us to choose a small number of strips to reduce the computational time without significantly affecting the final results. Disturbed clusters are expected to show higher values of the parameter because of the substructures (visible as off-centre peaks in the strips) or possible asymmetries.

3.2.7 *Gaussian fit parameter,* G

The Gaussian fit parameter G is based on a two-dimensional Gaussian fitting of the SZ maps applied within the aperture radius. The Gaussian model used can be written in terms of x and y coordinates as

$$f(x,y) = z_0 + A\,\exp\left\{-[a(x-x_0)^2 + 2b(x-x_0)(y-y_0)^2 + c(y-y_0)]\right\}, \tag{13}$$

where a, b and c are constants defined as

$$a = \frac{\cos^2\theta}{2\sigma_x^2} + \frac{\sin^2\theta}{2\sigma_y^2}$$
$$b = -\frac{\sin 2\theta}{4\sigma_x^2} + \frac{\sin 2\theta}{4\sigma_y^2}$$
$$c = \frac{\sin^2\theta}{2\sigma_x^2} + \frac{\cos^2\theta}{2\sigma_y^2}. \tag{14}$$

The best-fitting parameters obtained from the procedure are the following: the angle θ between the axes of the map and those of the bi-dimensional Gaussian distribution; the coordinates of the peak of the model map, x_0 and y_0; its amplitude A; the offset z_0 and the two standard deviations, σ_x and σ_y. The G parameter is just defined as the ratio:

$$G = \frac{\sigma_{\rm min}}{\sigma_{\rm max}}, \tag{15}$$

where $\sigma_{\rm min}$ ($\sigma_{\rm max}$) denotes the smallest (largest) value between σ_x and σ_y. We expect lower values of G for disturbed clusters, which should show asymmetric shapes, resulting in significantly different standard deviations along the x and y directions in the Gaussian fit. G should be close to 1 for regular clusters. We stress that, like the centroid shift, this parameter could lead to a misclassification of disturbed clusters with symmetrically distributed substructures. Also note that the aperture radius within which the fit is computed should be sufficiently large, to take into account possible substructures far from the centre.

To illustrate how the new strip and Gaussian parameters work, we show their different behaviours for an example of a relaxed and a disturbed cluster (clusters 7 and 27, respectively) from the radiative subset at $z = 0.54$. Fig. 1 shows the strips defined as above. As expected, the four profiles for the relaxed cluster are similar at all radii ($S = 0.09$). In contrast, multiple off-centre peaks characterize the profiles of the disturbed cluster, corresponding to substructures ($S = 0.4$). Fig. 2 illustrates the maps of the two clusters and the contour lines representing the Gaussian fit to the maps. The difference between the relaxed and the unrelaxed cluster can be seen from the shapes of the contour lines, which are nearly circular in the first case ($G = 0.97$) and elliptical in the second case ($G = 0.63$).

3.2.8 *Combined parameter,* M

Finally, we introduce a combined parameter called M (see also Rasia et al. 2013; Meneghetti et al. 2014), where each of the previously defined parameters, denoted generically as V_i, contributes to M according to a weight W_i, related to the efficiency of V_i in discriminating the dynamical state, as will be detailed later in Section 4.2. The analytical definition of the combined parameter is, thus:

$$M = \frac{1}{\sum_i W_i}\left(\sum_i W_i \frac{\log_{10}(V_i^{\alpha_i}) - \langle\log_{10}(V_i^{\alpha_i})\rangle}{\sigma_{\log_{10}(V_i^{\alpha_i})}}\right), \tag{16}$$

where the sums extend over all the parameters, and α_i is equal to +1 when disturbed clusters are associated with large values of V_i (e.g. as for A), otherwise it is equal to −1 (e.g. like for c). The brackets $\langle\rangle$ indicate the average computed over all the clusters and σ is the standard deviation. By definition, we expect negative values for relaxed clusters and positive values for disturbed ones.

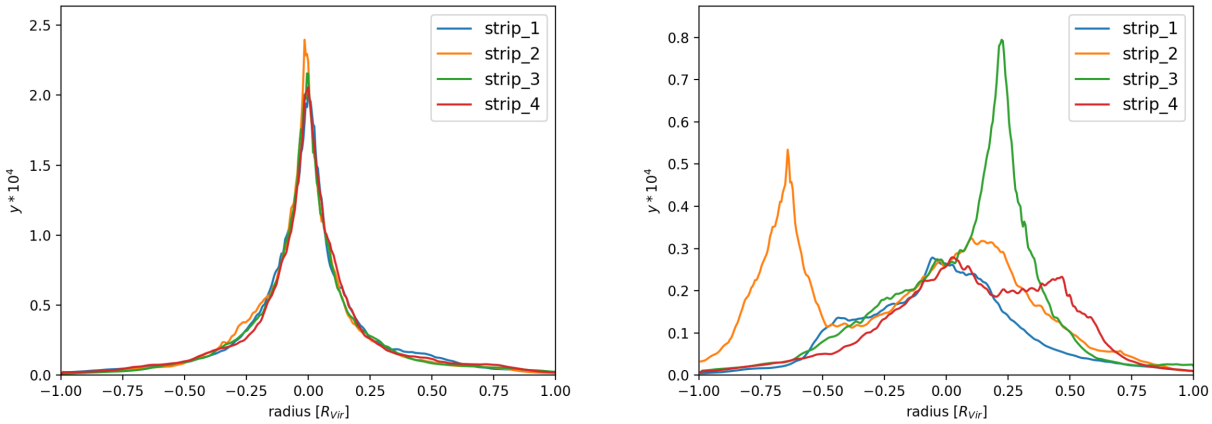

Figure 1. Strips passing through the centroid of the SZ maps of a relaxed cluster (cluster 7, left) and of an unrelaxed one (cluster 27, right) for the four chosen orientations (see text for a description) at red shift $z = 0.54$ for the CSF flavour. The corresponding values of the S parameter for the two clusters are 0.09 and 0.40, respectively.

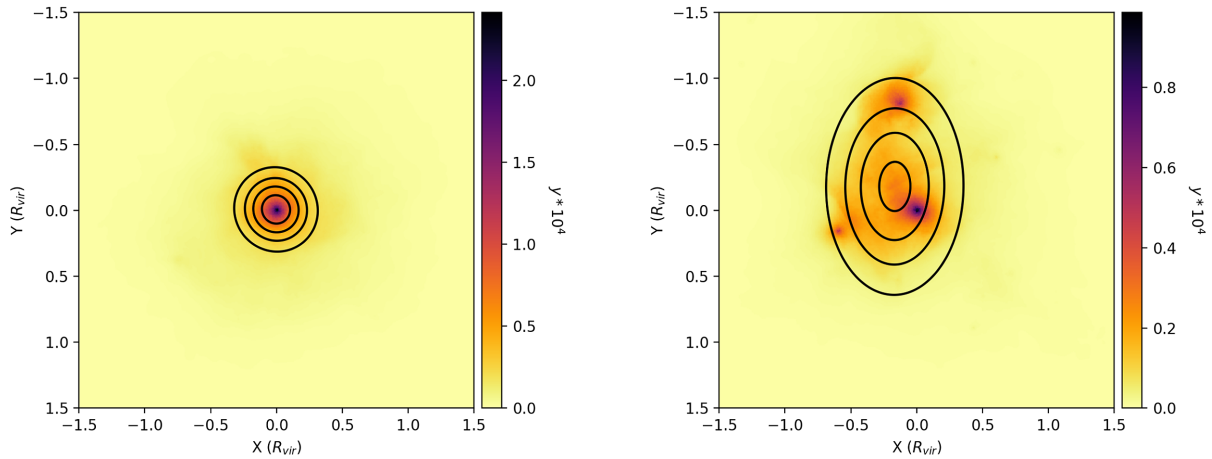

Figure 2. Best Gaussian fit contour lines (at 20, 40, 60 and 80 per cent of the maximum y value), resulting from the computation of the G parameter. Contours are superimposed on the SZ maps of the example relaxed cluster (cluster 7, left) and disturbed cluster (cluster 27, right) at red shift $z = 0.54$ from the CSF subset. The corresponding values of the G parameter are 0.97 and 0.63 for the two clusters, respectively.

4 RESULTS

In this section we first discuss the efficiency of the parameters described in Section 3.2, then we analyse their stability by varying the observer line of sight (and thus, we consider multiple projections of the same cluster) and by changing the angular resolutions of the maps.

4.1 Application of the single parameters

We quantify the efficiency of the morphological parameters with a Kolmogorov–Smirnov (KS) test on the distributions of the two populations of relaxed and disturbed objects, as identified from the 3D indicators of the cluster dynamical state (see Section 3.1). From this test, we obtain the probability p that they belong to the same sample. Low values of this probability indicate an efficient discrimination between the two populations.

For all the parameters, the efficiency depends on the aperture radius $R_{\rm ap}$ and in a few cases, also on the inner radius, such as for the light concentration ratio, or on the FWHM for the fluctuation parameter. As described in the previous section, we consider multiple values for all these quantities, and we finally chose those that correspond to the lower value of the probability p, averaged over the four red shifts and two sub-samples. The fluctuation parameter returned contradictory results for the red shifts and physics, demonstrating that it is not a stable parameter. For this reason, it will be discarded from the rest of the analysis. The minimum probability values for each parameter are listed in Table 2, where we also present the superimposition percentage $s_{\rm p}$ of the distributions of the two populations and the most efficient aperture radius. The latter is $R_{\rm ap} = 0.75R_{\rm vir}$ for the asymmetry parameter, $R_{\rm ap} = 0.25R_{\rm vir}$ for the light concentration ratio and $R_{\rm ap} = R_{\rm vir}$ for all the others.

In general, we find small values for the KS probability, so we can conclude that the relaxed and disturbed populations do not coincide. This implies there is good agreement between the dynamical state expected from the 3D indicators and the one inferred from the parameters. Since the results are similar for the NR and the CSF flavours, we conclude that gas radiative processes do not have a significant impact on the SZ maps on which the parameters are computed (consistent with e.g. Motl et al. 2005). The differences are also negligible, within a few per cent, in terms of red-shift variation.

The light concentration ratio, for which the best inner radius is $r_{\rm l} = 0.05R_{\rm vir}$, has the smallest overlap between the two classes,

Table 2. Results from the application of the A, c, $\log_{10}(P_3/P_0)$, w, G and S parameters to the SZ maps of the sample, for the four analysed red shifts and the two flavours of the simulation. R_{ap} is the best aperture radius as derived from the minimum KS test probability, p_m. s_p is the superimposition percentage of the distributions of the parameters for the two populations.

		CSF		NR	
R_{ap} (R_{vir})	z	s_p per cent	p_m	s_p per cent	p_m
			A		
0.75	0.43	55	8.7×10^{13}	59	6.7×10^{10}
	0.54	50	8.5×10^{17}	49	1.4×10^{14}
	0.67	58	1.8×10^{11}	63	1.2×10^{09}
	0.82	61	9.2×10^{12}	53	6.8×10^{13}
			c		
0.25	0.43	51	4.8×10^{14}	57	2.3×10^{13}
	0.54	47	2.0×10^{16}	53	5.9×10^{13}
	0.67	47	6.8×10^{17}	52	3.8×10^{16}
	0.82	48	4.2×10^{16}	57	3.0×10^{12}
			$\log_{10}(P_3/P_0)$		
1.00	0.43	65	3.8×10^{06}	69	1.4×10^{05}
	0.54	75	8.5×10^{03}	72	4.0×10^{03}
	0.67	62	3.5×10^{09}	65	2.7×10^{08}
	0.82	64	4.8×10^{09}	67	2.6×10^{06}
			w		
1.00	0.43	53	5.0×10^{11}	53	2.0×10^{11}
	0.54	57	3.5×10^{11}	46	5.9×10^{18}
	0.67	54	1.0×10^{11}	59	7.0×10^{11}
	0.82	55	9.7×10^{13}	55	1.5×10^{10}
			S		
1.00	0.43	47	1.3×10^{16}	52	1.4×10^{12}
	0.54	57	1.5×10^{11}	66	4.3×10^{09}
	0.67	66	3.1×10^{08}	63	2.7×10^{08}
	0.82	60	1.5×10^{10}	62	4.2×10^{10}
			G		
1.00	0.43	70	1.4×10^{04}	73	3.5×10^{03}
	0.54	60	5.7×10^{10}	71	7.4×10^{05}
	0.67	58	2.6×10^{09}	72	5.9×10^{04}
	0.82	68	1.3×10^{05}	67	3.9×10^{05}

especially for the CSF flavour (about or less than 50 per cent). In our sample, this parameter and the centroid shift are the most efficient, as found also in Lovisari et al. (2017). The asymmetry parameter, with a superimposition percentage around 55 per cent, is the third most efficient parameter. On the other hand, the third-order power ratio, widely used on X-ray maps (see e.g. Rasia et al. 2013), shows a wide overlap between the two populations (around 65 per cent, reaching an extreme of 75 per cent). The different response of the power ratio on SZ maps with respect to X-ray maps is mostly caused by its strong dependence on the signal-to-noise ratio (Poole et al. 2006) or the gradient of the signal. In SZ, it is particularly affected by the instrumental beam (see e.g. Donahue et al. 2016). Since we have not accounted for all the aspects that may strongly depend on the detection instrument, our conclusions regarding P_3/P_0 are still not applicable to observational results.

Of the two new parameters we have introduced, the strip parameter performs better than the Gaussian fitting parameter. This is also evident by comparing Figs 3 and 4, where the large overlapping area and the two populations in the G histogram are remarkable. The inefficiency of this parameter is mostly because the Gaussian fitting

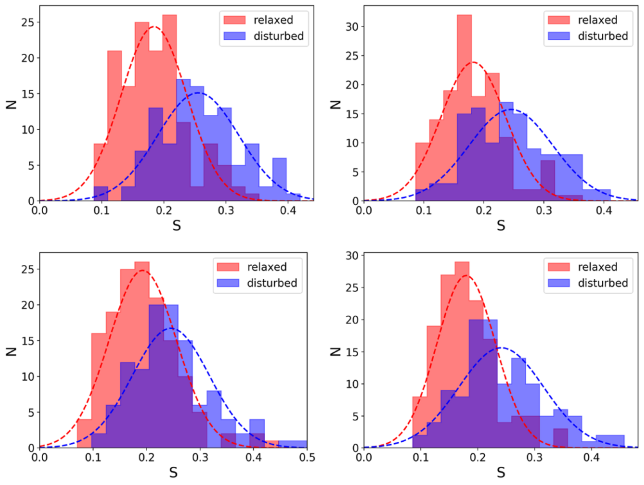

Figure 3. Distribution of S computed inside $R_{ap} = R_{vir}$ for the four different red shifts (0.43 top left, 0.54 top right, 0.67 bottom left and 0.82 bottom right) and for the CSF flavour. The red and blue bars indicate the relaxed and unrelaxed populations, respectively, from the a priori discrimination through the 3D indicators. The dashed lines are the Gaussian fits of the relaxed (red) and disturbed (blue) populations.

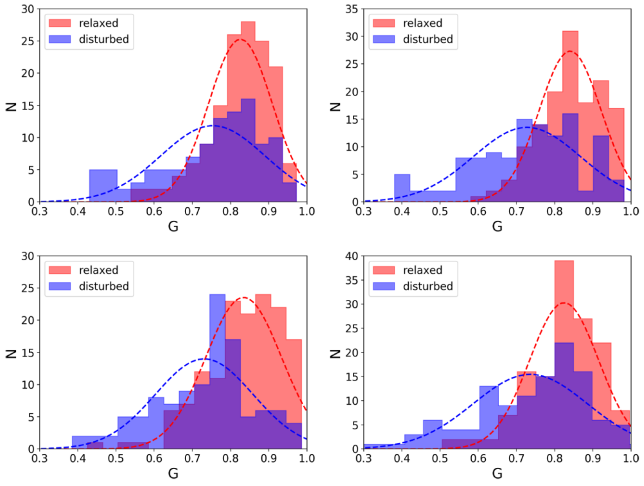

Figure 4. Distribution of the G parameter computed inside $R_{ap} = R_{vir}$ for the CSF flavour (red shift 0.43 top left, 0.54 top right, 0.67 bottom left and 0.82 bottom right). The red and blue bars indicate the relaxed and disturbed populations while the red and blue dashed lines are the Gaussian fits for the relaxed and disturbed populations.

procedure smooths and reduces the impact of small substructures and G is mainly affected by projection effects. Indeed, a dynamically disturbed cluster may appear regular when smoothed and observed from a particular line of sight. This effect leads to a conspicuous fraction of disturbed clusters being identified as relaxed.

4.1.1 *Comparison with X-ray results*

We compare our morphological parameters, c, w and $\log(P_3/P_0)$, with those measured in the mock X-ray *Chandra*-like maps described in Section 2.1. For a fair comparison, we re-compute the SZ morphological parameter on the same sub-sample of the MUSIC clusters used for the X-ray analysis. The sample includes clusters from the radiative data set at red shifts $z = 0.43$ and $z = 0.67$ observed from three different lines of sight. We also set the same

Table 3. Pearson correlation coefficients between the X-ray and SZ results for the three parameters compared, c, w and $\log(P_3/P_0)$, at red shifts 0.43 and 0.67.

Parameter	All	Relaxed	Disturbed
	$z = 0.43$		
c	0.45	0.73	0.18
$\log_{10}(P_3/P_0)$	0.14	0.38	0.12
w	0.02	0.23	−0.31
	$z = 0.67$		
c	0.61	0.73	0.41
$\log_{10}(P_3/P_0)$	0.25	0.29	0.09
w	0.05	0.46	−0.30

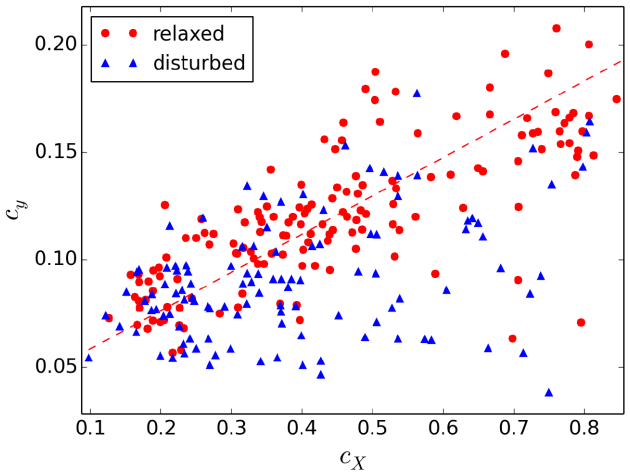

Figure 5. Scatter plot of the c parameter computed on X-ray (c_X) and SZ maps (c_y) for the NR clusters at $z = 0.67$. Relaxed clusters are marked as red circles and disturbed ones are marked as blue triangles. The red dashed line shows the best robust fit for the relaxed clusters only.

aperture radii equal to 500 kpc. Finally, for the light concentration ratio c, we use an inner radius of 100 kpc.

Table 3 reports the Pearson correlation coefficients between the X-ray and the SZ results, computed for the three parameters on three samples: one considering all the clusters, and two subsets built from the relaxed and disturbed populations, respectively. The correlation is high only for the light concentration ratio, whose corresponding scatter plot is shown in Fig. 5. In addition to the correlation, notice the significant difference in the dynamic range of the X-ray and SZ parameters caused by the different dependence of the two signals on the electron density, which is more peaked in X-ray. As expected, the two power ratios correlate poorly given the opposite performances of this parameter in the two bands. No significant correlation is present also for the centroid shift, probably because of the SZ and X-ray dependence on the peaked density of possible substructures. A similar comparison was performed by Donahue et al. (2016), based on the application of the parameters on maps of the CLASH sample (see Section 1 and Postman et al. 2012), but applying in the SZ maps the same centre position and outer radii used for the X-ray analysis. Also in this work, the concentration parameters show a good correlation despite their different dynamic ranges.

Table 4. Average over the red shifts and flavours of the weights for the single parameters used in the definition of the M parameter.

Parameter	W_i
A	9.63
c	12.31
$\log_{10}(P_3/P_0)$	2.80
w	10.38
S	8.10
G	3.31

4.2 Application of the combined parameter

We compute the combined morphological parameter M, introduced in Section 3.2.8, following equation (16). Each V_i parameter is measured within its most efficient aperture radius (Table 2), and its weight W_i is the absolute value of the logarithm of the corresponding KS probability p_i, averaged over the four red shifts and two cluster subsets (Table 4):

$$W_i = |\log_{10}(p_i)|. \quad (17)$$

With this choice, the parameters showing a higher efficiency (i.e. with low values of p_i) contribute the most to M. The heaviest parameters are the light concentration ratio and the centroid shift. In contrast, P_3/P_0 has the least influence. This suggests that this parameter could be neglected in real applications for observed SZ maps, without affecting significantly the final value of M.

The distributions of M for the relaxed and unrelaxed clusters are shown in Fig. 6. The corresponding overlap percentages and probabilities from the KS test are listed in Table 5. Notice the efficiency improvement of this parameter over each single parameter. The contamination level is of the order of 22 per cent for the relaxed population and 28 per cent for the disturbed population.

4.3 Test of the stability of the parameters

To check the stability of all parameters, we produce SZ maps of two relaxed and two disturbed clusters from our CSF subset at $z = 0.54$ and $z = 0.82$ along 120 lines of sight. We checked that the results are similar for the NR subset and at the remaining red shifts. Specifically, we consider lines of sight spaced in uniform steps of 9°. The six morphological parameters and the combined one are applied to all these maps and their distributions are drawn. The corresponding standard deviations are an estimate of the stability of the parameter. We list the results in Table 6. For all parameters, disturbed clusters tend to have a higher dispersion with respect to the relaxed ones, as expected because of projection effects. The mean value of the standard deviation of M, with respect to the four clusters at both red shifts, is $\langle\sigma_M\rangle = 0.41$. We consider this value as the uncertainty of the M parameter. For this reason, all clusters with M between −0.41 and 0.41 might be a mix of relaxed and disturbed objects.

4.4 Effects of the angular resolution

Current SZ experiments cannot reproduce the angular resolution of our maps (see Section 1). In this section, we verify the impact of the resolution on the performance of the morphological parameters. We, thus, reduce the SZ signal of our maps by applying a Gaussian smoothing. We choose three FWHMs similar to the typical resolution achieved by existing telescopes in the millimetric

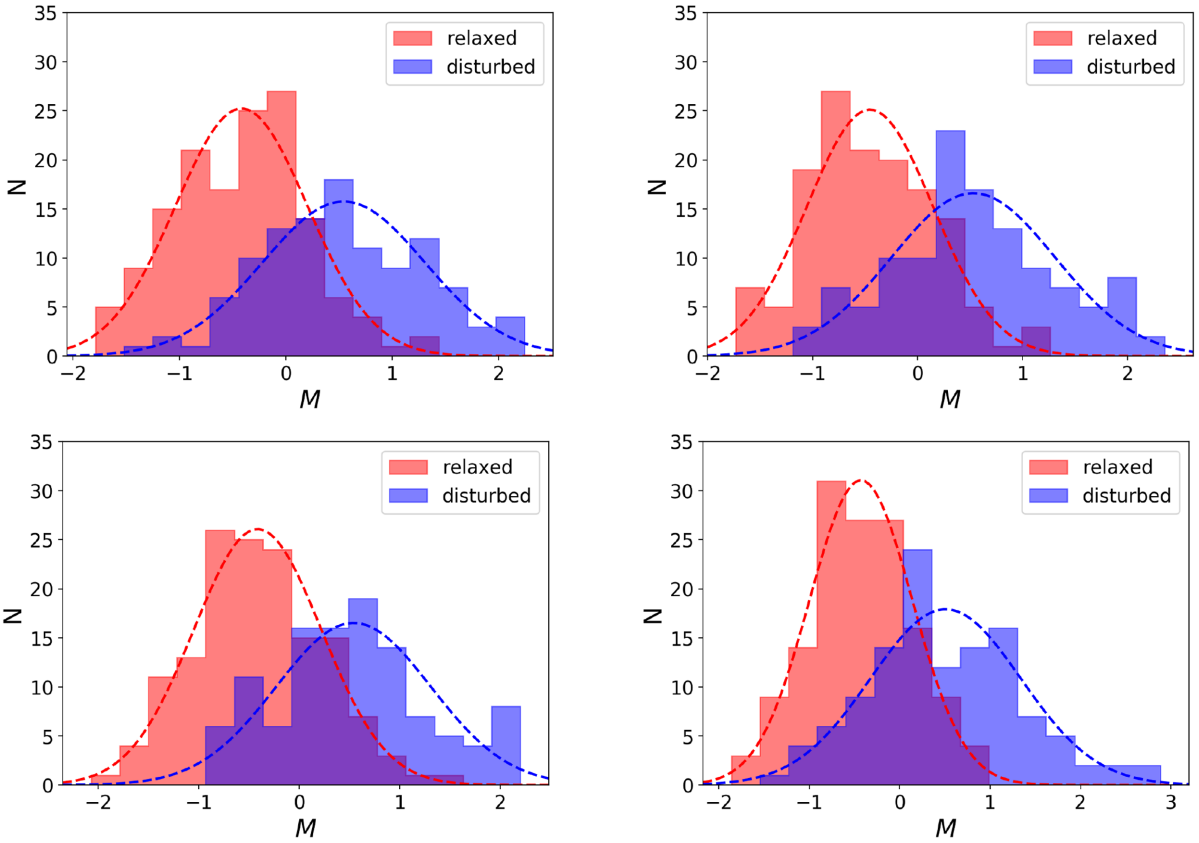

Figure 6. Distributions of M computed with KS suggested aperture radii at the four different red shifts (0.43 top left, 0.54 top right, 0.67 bottom left and 0.82 bottom right) for the CSF flavour. The red and blue bars indicate the relaxed and unrelaxed populations respectively, determined from the 3D indicators.

Table 5. Superimposition percentage s_p between the distributions of relaxed and disturbed clusters, and associated KS probability p_m for the M parameter.

	CSF		NR	
z	s_p per cent	p_m	s_p per cent	p_m
0.43	47	4.2×10^{18}	50	3.0×10^{14}
0.54	45	7.7×10^{19}	48	2.5×10^{16}
0.67	51	1.3×10^{16}	51	1.2×10^{13}
0.82	49	3.8×10^{16}	51	1.0×10^{14}

band: 20 arcsec for IRAM 30-m telescope, 1 arcmin for SPT 10-m telescope and 5 arcmin for the *Planck* telescope. We perform the convolution only on CSF maps at $z = 0.54$ and $z = 0.82$.

The superimposition percentages of the histograms of the relaxed and unrelaxed classes for the M parameter are listed in Table 7. The overlap is expected to increase with the FWHM (i.e. with increasing resolution). Nevertheless, we find a decrease of 1 and 3 per cent of the superimposition at 20 arcsec and 1 arcmin, respectively. This may be explained by considering that the M parameter depends on the overall morphology, thus small-scale effects are negligible at resolutions of the order of a few arcminutes. With respect to the individual parameters, we found that the angular resolution barely affects their ability to distinguish between the two dynamical classes when the morphological parameters are sensitive to the properties of the cluster core, such as the light concentration ratio. Moreover, the resolution has a large impact on the results derived from the parameters built to enhance the presence of substructures such as the strip parameter.

5 MORPHOLOGY AND HYDROSTATIC MASS BIAS

We investigate, here, the correlation between the morphological parameter M and the deviation from the hydrostatic equilibrium in the ICM. For each simulated cluster, we define the hydrostatic mass bias as

$$b_M = \frac{(M_{500,\mathrm{HSE}} - M_{500})}{M_{500}}. \quad (18)$$

In the expression above, M_{500} is the mass obtained by summing the gas and DM particles inside R_{500}. $M_{500,\mathrm{HSE}}$ is the mass computed under the assumption of hydrostatic equilibrium, expressed as

$$M_{500,\mathrm{HSE}} = -\frac{k_B T r}{G \mu m_H} \left(\frac{\mathrm{d} \ln \rho}{\mathrm{d} \ln r} + \frac{\mathrm{d} \ln T}{\mathrm{d} \ln r} \right), \quad (19)$$

where k_B and G are the Boltzmann and gravitational constants, r is the radius from the centre of the cluster, μ is the mean molecular weight, m_H the hydrogen mass, ρ the density and T the mass-weighted temperature (Sembolini et al. 2013). The mass bias has been analysed in many works on hydrodynamical simulations, lensing and X-ray observations, like Kay et al. (2004), Rasia et al. (2006), Nagai, Vikhlinin & Kravtsov (2007), Jeltema et al. (2008), Piffaretti & Valdarnini (2008), Zhang et al. (2010), Meneghetti et al. (2010), Becker & Kravtsov (2011) and Sembolini et al. (2013).

The sources of the asymmetry in the ICM distribution should also impact the hydrostatic equilibrium. We, therefore, investigate the correlation between the absolute value of the mass bias $|b_M|$ and the M parameter in our sample. The results are reported in Fig. 7 for CSF clusters (NR clusters have a similar behaviour). For

Table 6. Standard deviations of all morphological parameters for two relaxed clusters (17 and 267) and two disturbed clusters (44 and 277) at red shifts 0.54 and 0.82, as derived from the SZ maps computed for 120 different lines of sight.

Parameter	$z = 0.54$				$z = 0.82$			
	Relaxed		Disturbed		Relaxed		Disturbed	
	Cluster 17	Cluster 267	Cluster 44	Cluster 277	Cluster 17	Cluster 267	Cluster 44	Cluster 277
A	0.030	0.040	0.060	0.050	0.060	0.040	0.100	0.080
c	0.007	0.002	0.008	0.013	0.014	0.005	0.008	0.015
$\log_{10}(P_3/P_0)$	0.620	0.430	0.600	0.430	0.470	0.630	0.400	0.510
w	0.002	0.0007	0.004	0.003	0.001	0.001	0.005	0.008
S	0.030	0.020	0.060	0.020	0.040	0.020	0.070	0.040
G	0.070	0.060	0.050	0.070	0.040	0.070	0.070	0.130
M	0.28	0.30	0.43	0.37	0.49	0.26	0.57	0.58

Table 7. Superimposition percentages of M with respect to the FWHM of the Gaussian filter applied to the maps to simulate a decreasing angular resolution.

	z	
FWHM (arcsec)	0.54 per cent	0.82 per cent
20	43	48
60	41	46
300	51	54

each red shift and simulated subset (NR or CSF), we compute the Pearson correlation coefficient and report the results in Table 8. This coefficient is almost always below 0.30. This rather weak correlation leads us to conclude that there is no strong connection between $|b_{\rm M}|$ and the morphology of the cluster as quantified by our indicators.

This result suggests that the amplitude of the mass bias is not tightly connected to the dynamical state of a cluster. However, we stress that the mass bias we used for this comparison was computed within R_{500}. This may be a limiting factor, since a different radial value could be used. For this reason, we compute the median profiles of the mass bias along the cluster radius, for the relaxed and disturbed clusters segregated according to the 3D parameters. We show these profiles in Fig. 8. A consistent superimposition between the two populations within the median absolute deviation can be seen from $0.8R_{500}$ and beyond. It can also be seen that the scatter of the median profile for the disturbed clusters is higher, since they are expected to show a more significant deviation from the hydrostatic equilibrium with respect to the relaxed ones. Among others, Biffi et al. (2016) investigated the median radial profile of the mass bias, using a small sample of six relaxed and eight disturbed clusters from a simulation, which also includes feedback from active galactic nuclei. They found that the radial median profiles of the relaxed and disturbed clusters have very small differences, as in our case, and that the mass bias is slightly lower (in absolute value) for the relaxed clusters.

6 MORPHOLOGY AND PROJECTED SZ-CM OFFSET

An additional indicator of the dynamical state, which can be computed from observations, is the offset between the positions of the BCG and the X-ray peak. The goodness of this parameter to infer the dynamical state has been proven through the years by both observations (see e.g. Katayama et al. 2003; Patel et al. 2006; Donahue et al. 2016; Rossetti et al. 2016) and simulations (see e.g. Skibba & Macciò 2011). An equivalent indicator on SZ maps has recently been investigated by Gupta et al. (2017) using the *Magneticum* simulation. Indeed, they computed the projected offset between the centre of the gravitational potential of a cluster and the SZ peak, normalized to R_{500}.

We compute the projected offset $D_{y-\rm CM}$ between the centroid of the y-map inside $R_{\rm vir}$ and the CM of the cluster (which, at a first approximation, coincides with the BCG), normalized to $R_{\rm vir}$. The correlation between $D_{y-\rm CM}$ and our combined morphological parameter is then analysed, to compare pure morphological information with an observational dynamical state-driven quantity. The correlation is of the order of 80 per cent, as shown in Table 9. Fig. 9 shows the correlation for the CSF subset. No significant deviations are found in the NR sample. The strong correlation between M and $D_{y-\rm CM}$ suggests that morphology is closely related to the dynamical state. Therefore, under the assumption of a coincidence between the CM and BCG positions, this parameter can be easily inferred from joint optical and SZ observations. Since the threshold for the M parameter is known, we derive the corresponding average threshold for $D_{y-\rm CM}$ of 0.070 by interpolating the best-fitting curve. This allows us to infer that a cluster is relaxed (unrelaxed) if $D_{y-\rm CM}$ is below (above) this value. Moreover, this threshold is consistent with that found by Meneghetti et al. (2014) by referring to the 3D offset between the position of the CM and the minimum of the gravitational potential. Following the same approach used for the analysis of the M parameter contaminants, we find that there is an average of 25 per cent (20 per cent) contaminant clusters in the relaxed (disturbed) population. Since this contamination is lower than the corresponding one for the M parameter, we conclude that this 2D offset performs better in discriminating the dynamical state of the clusters. Considering the average deviation of M, $\langle\sigma_{\rm M}\rangle = 0.41$, we derive through an interpolation the corresponding deviation of $D_{y-\rm CM}$ of $\langle\sigma_{\rm D}\rangle = 0.029$. Hence, as a final criterion, we consider a cluster to be relaxed if $D_{y-\rm CM} < 0.041$ and disturbed if $D_{y-\rm CM} > 0.099$.

7 CONCLUSIONS

Studying cluster morphology through several indicators allows us to analyse large amounts of data from surveys in different spectral bands and will be crucial in understanding the structure formation scenario. This topic has been studied in the X-ray band, and we approach it here for the first time using SZ maps, opening a new window on cluster morphology in the microwave band. Thus, we analysed the application of some morphological parameters on the synthetic SZ maps of ∼260 massive clusters extracted from

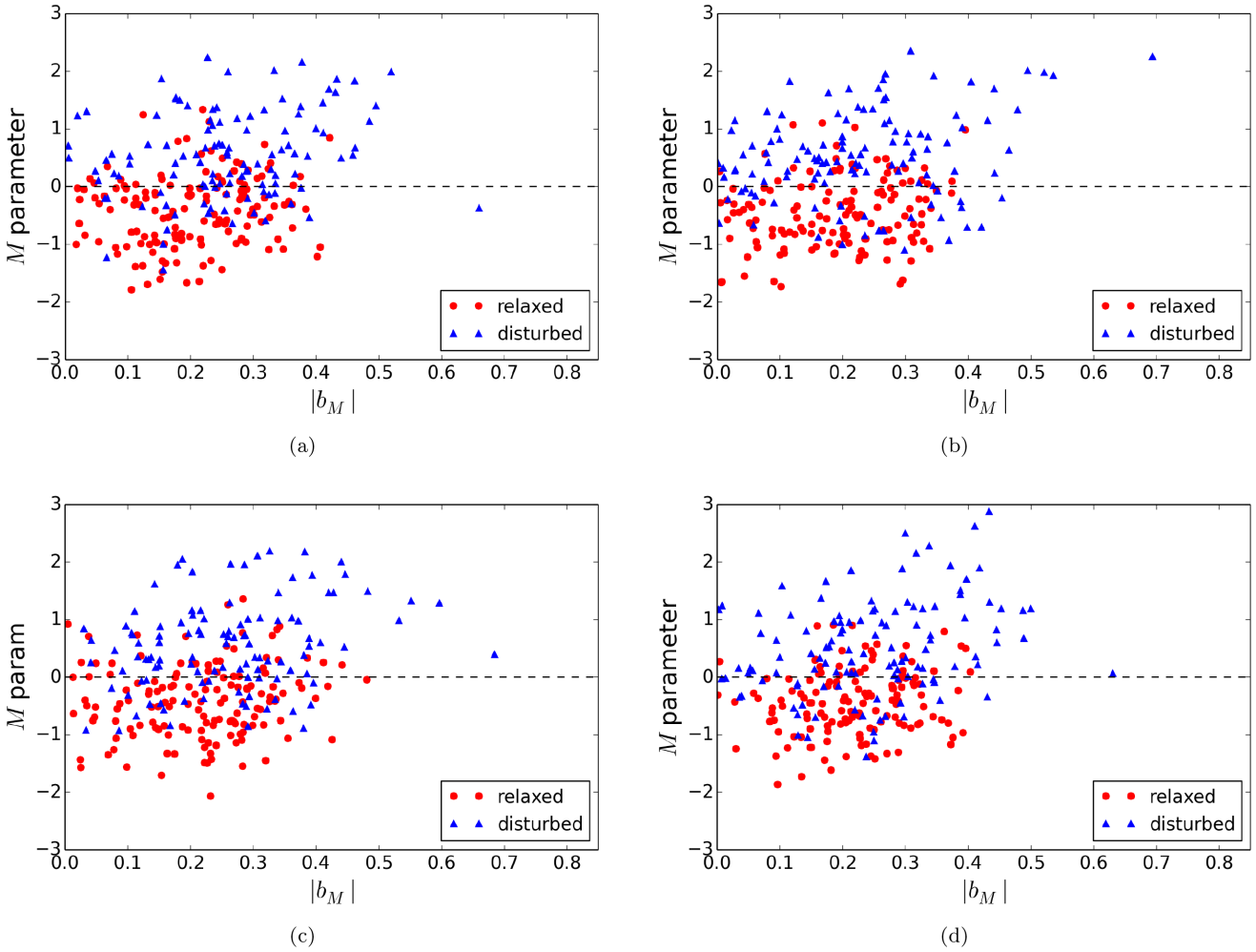

Figure 7. Absolute value of the mass bias $|b_M|$ plotted against the M combined parameter for the CSF flavour at red shifts 0.43, 0.54, 0.67 and 0.82 (shown in panels (a), (b), (c) and (d), respectively). Relaxed and disturbed clusters are marked with red filled circles and blue filled triangles, respectively. The black dashed line marks the threshold ($M = 0$) for the M parameter.

Table 8. Pearson correlation coefficients found between $|b_M|$ and M for all considered red shifts and flavours.

z	Pearson correlation coefficient	
	CSF	NR
0.43	0.29	0.28
0.54	0.27	0.29
0.67	0.26	0.30
0.82	0.27	0.37

the MUSIC-2 data set, taking non-radiative and radiative physical processes into account, and studying four different red shifts. The clusters have been a priori classified as relaxed or disturbed using two standard 3D theoretical indicators: Δ_r and $M_{\rm sub}/M_{\rm vir}$. These are related, respectively, to the offset between the peak of the density distribution and the CM, and to the mass ratio between the biggest substructure and the total halo. We use a set of observational parameters derived from the X-ray literature and two new ones (the Gaussian fit and the strip parameters), testing their performance when applied on SZ maps in terms of efficiency and stability. The parameters were properly combined into a single morphological estimator M. The discriminating power of M was found to be higher

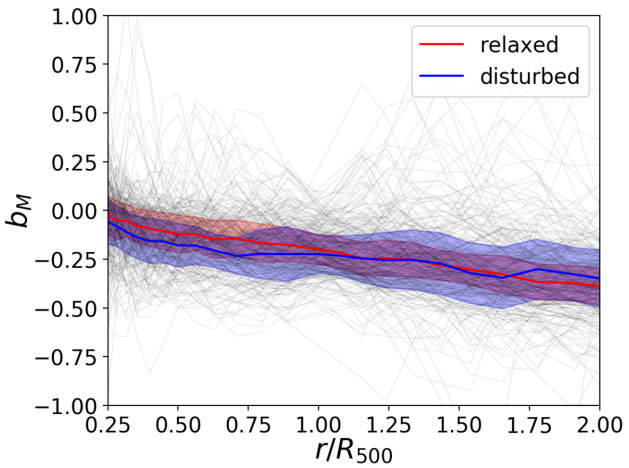

Figure 8. Radial median profiles of b_M for relaxed (red) and disturbed (blue) clusters of the sample at red shift $z = 0.54$ and CSF flavour. Grey shaded lines represent the highly scattered single cluster profiles from which the median is computed. The coloured regions indicate the median absolute deviations of the median profiles.

Table 9. Pearson correlation coefficients between $D_{y-\mathrm{CM}}$ and the M combined parameter for all the analysed red shifts and flavours.

z	Pearson correlation coefficient	
	CSF	NR
0.43	0.78	0.78
0.54	0.77	0.75
0.67	0.76	0.79
0.82	0.75	0.75

than that of the single parameters. Moreover, we studied its possible correlations with the hydrostatic mass bias and with the projected offset between the position of the SZ peak and the position of the CM of the cluster.

Our results can be summarized as follows:

(i) A few of the morphological parameters (namely the light concentration, the centroid shift and the asymmetry) are as efficient when applied to SZ maps as they are for X-ray maps. This may be because of their sensitivity to the very central core region morphology, which has been probed well both in SZ and in X-ray imaging. Nevertheless, other parameters have been proven to be less efficient for X-ray maps, such as e.g. the third-order power ratio and the fluctuation parameter, which, in particular, shows unexpected behaviour in our case.

(ii) The combined parameter M has a smaller overlap of the two dynamical state populations than any of the single parameters. Its threshold value $M = 0$ properly discriminates between relaxed and disturbed dynamical states. The contaminant percentages are 22 per cent for disturbed clusters and 28 per cent for relaxed clusters, respectively. We have estimated the error for the parameter as the standard deviation, computed from the estimation of M on maps projected along many different line of sight, finding it to be $\overline{\sigma_{\mathrm{M}}} = 0.41$.

(iii) By varying the angular resolution of the maps using Gaussian smoothing, the overlap of the two populations determined through the combined parameter shows an expected increase at the lowest resolution we tested (5 arcmin). Nevertheless, when the resolution is below or equal to 1 arcmin, the performance improves. This may be because of the suppression of small fluctuations on the maps due to the convolution with the beam resolution.

(iv) The M parameter, which has been proven to be a good proxy of the dynamical state, shows a weak correlation with the mass bias, in agreement with other analyses in the literature.

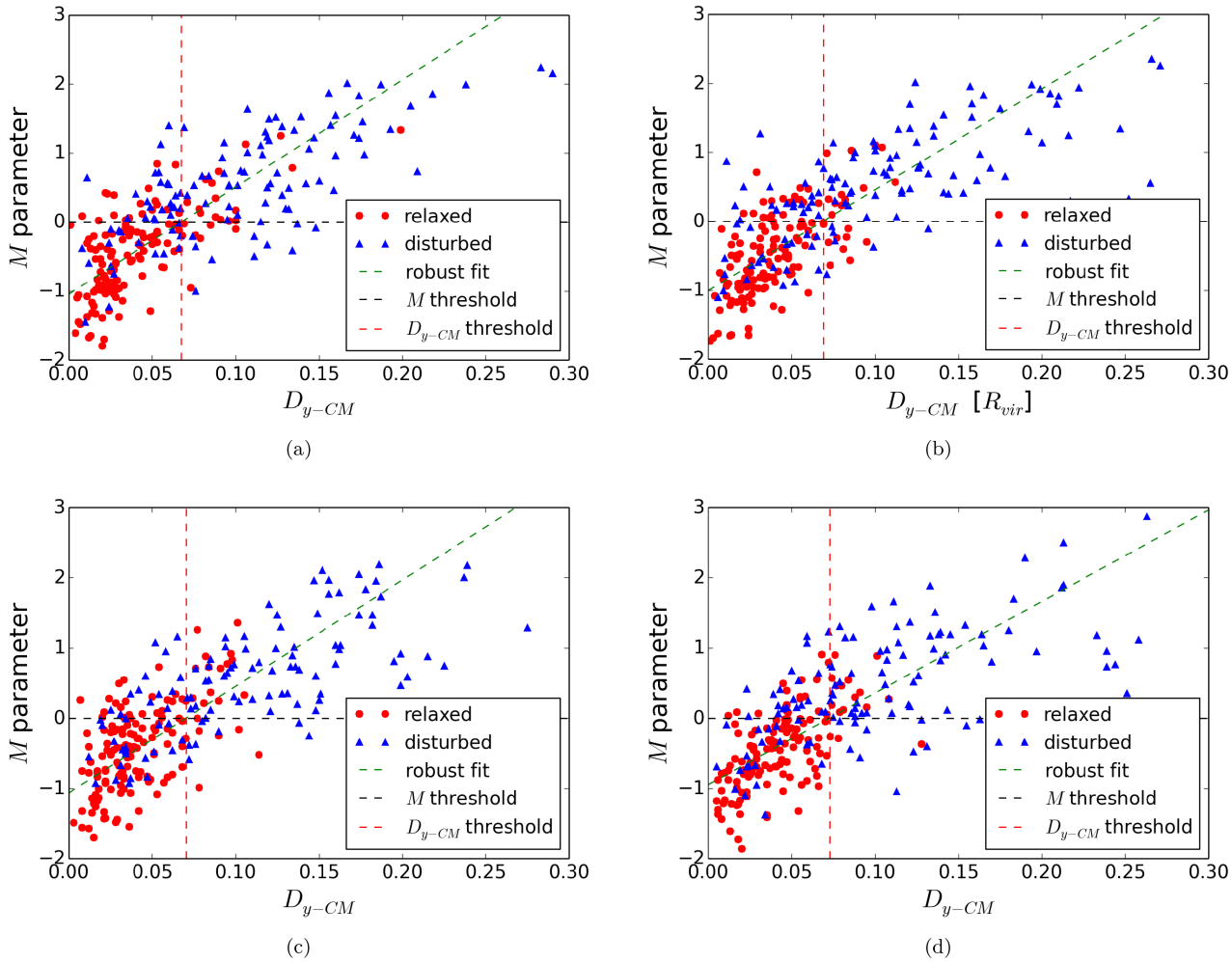

Figure 9. Scatter plots of the $D_{y-\mathrm{CM}}$ 2D offset versus the combined parameter M. Panels (a), (b), (c) and (d) refer to red shifts 0.43, 0.54, 0.67 and 0.82, respectively. Black horizontal and red vertical dashed lines mark the M and $D_{y-\mathrm{CM}}$ thresholds, respectively. Green dashed lines show the best robust fit for all clusters.

(v) The 2D spatial offset $D_{y-\mathrm{CM}}$ between the SZ centroid and CM of a cluster is strongly correlated with its morphology and dynamical state, with a correlation coefficient of ∼80 per cent. This correlation shows no significant dependence on the cluster red shift or on the simulation flavour. We propose this indicator as a fast-to-compute observational estimator of a cluster's dynamical state. From the threshold of 0.070 – inferred by interpolating on the best-fitting relation linking $D_{y-\mathrm{CM}}$ with M – we get a contamination of 25 and 20 per cent for the relaxed and disturbed samples, respectively. This reduced contamination suggests this parameter has slightly better segregating power compared with M. As a final criterion to distinguish between the two populations, we conclude that a cluster having $D_{y-\mathrm{CM}} < 0.041$ can be classified as relaxed and as non-relaxed if $D_{y-\mathrm{CM}} > 0.099$.

We plan to apply the analysis outlined in this work to more realistic data, namely by processing the current synthetic maps through the NIKA-2 instrument pipeline, to take the impacts of astrophysical and instrumental contaminants into account.

ACKNOWLEDGEMENTS

The authors wish to thank the referee, G. B. Poole, for the constructive and useful comments, which improved this paper significantly, and they acknowledge V. Biffi for useful discussions. This work has been partially supported by funding from Sapienza University of Rome (Progetti di Ricerca Anno 2015 prot. C26A15LXNR). The MUSIC simulations have been performed on the MareNostrum supercomputer at the Barcelona Supercomputing Centre, thanks to the computing time awarded by Red Española de Supercomputación. GY and FS acknowledge financial support from MINECO/FEDER under research grant AYA2015-63810-P. ER acknowledges the financial contribution from agreement ASI-INAF n 2017-14-H.0.

REFERENCES

Adam R. et al., 2014, A&A, 569, A66
Adam R. et al., 2018, A&A, 609, A115
Andrade-Santos F. et al., 2017, ApJ, 843, 76
Baldi A. S., De Petris M., Sembolini F., Yepes G., Lamagna L., Rasia E., 2017, MNRAS, 465, 2584
Becker M. R., Kravtsov A. V., 2011, ApJ, 740, 25
Biffi V., Sembolini F., De Petris M., Valdarnini R., Yepes G., Gottlöber S., 2014, MNRAS, 439, 588
Biffi V. et al., 2016, ApJ, 827, 112
Bleem L. E. et al., 2015, ApJS, 216, 27
Böhringer H. et al., 2010, A&A, 514, A32
Booth R. S., 2000, in Schürmann B., ed., ESA Special Publication Vol. 451, Darwin and Astronomy: the Infrared Space Interferometer. ESA, Noordwijk, The Netherlands, p. 107
Borgani S., 2008, in Plionis M., López-Cruz O., Hughes D., eds, Lecture Notes in Physics, Vol. 740, A Pan-Chromatic View of Clusters of Galaxies and the Large-Scale Structure. Springer-Verlag, Berlin, p. 24
Buote D. A., Tsai J. C., 1995, ApJ, 452, 522
Buote D. A., Tsai J. C., 1996, ApJ, 458, 27
Calvo M. et al., 2016, J. Low Temp. Phys., 184, 816
Carlstrom J. E., Holder G. P., Reese E. D., 2002, ARA&A, 40, 643
Cassano R., Ettori S., Giacintucci S., Brunetti G., Markevitch M., Venturi T., Gitti M., 2010, ApJ, 721, L82
Chang C. L. et al., 2009, AIPC, 1185, 475
Conselice C. J., 2003, ApJS, 147, 1
Cui W., Power C., Borgani S., Knebe A., Lewis G. F., Murante G., Poole G. B., 2017, MNRAS, 464, 2502
Czakon N. G. et al., 2015, ApJ, 806, 18
D'Onghia E., Navarro J. F., 2007, MNRAS, 380, L58
da Silva A. C., Kay S. T., Liddle A. R., Thomas P. A., Pearce F. R., Barbosa D., 2001, ApJ, 561, L15
Donahue M. et al., 2016, ApJ, 819, 36
Fabian A. C. ed., 1992, Proc. NATO Advanced Study Institute, NATO Advanced Science Institutes (ASI) Series C, Mathematical and Physical Sciences, Vol. 366. Kluwer, Dordrecht
Flores-Cacho I. et al., 2009, MNRAS, 400, 1868
Gardini A., Rasia E., Mazzotta P., Tormen G., De Grandi S., Moscardini L., 2004, MNRAS, 351, 505
George M. R. et al., 2012, ApJ, 757, 2
Giodini S., Lovisari L., Pointecouteau E., Ettori S., Reiprich T. H., Hoekstra H., 2013, Space Sci. Rev., 177, 247
Gómez P. L., Pinkney J., Burns J. O., Wang Q., Owen F. N., Voges W., 1997, ApJ, 474, 580
Gottlöber S., Yepes G., 2007, ApJ, 664, 117
Gupta N., Saro A., Mohr J. J., Dolag K., Liu J., 2017, MNRAS, 469, 3069
Haiman Z., Mohr J. J., Holder G. P., 2001, ApJ, 553, 545
Hallman E. J., Jeltema T. E., 2011, MNRAS, 418, 2467
Hasselfield M. et al., 2013, J. Cosmology Astropart. Phys., 7, 008
Jeltema T. E., Hallman E. J., Burns J. O., Motl P. M., 2008, ApJ, 681, 167
Johnston D. E. et al., 2007, preprint (arXiv:0709.1159)
Katayama H., Hayashida K., Takahara F., Fujita Y., 2003, ApJ, 585, 687
Kay S. T., Thomas P. A., Jenkins A., Pearce F. R., 2004, MNRAS, 355, 1091
Kitayama T. et al., 2016, PASJ, 68, 88
Klypin A., Kravtsov A. V., Bullock J. S., Primack J. R., 2001, ApJ, 554, 903
Klypin A., Yepes G., Gottlöber S., Prada F., Heß S., 2016, MNRAS, 457, 4340
Komatsu E. et al., 2011, ApJS, 192, 18
Lau E. T., Kravtsov A. V., Nagai D., 2009, ApJ, 705, 1129
Lovisari L. et al., 2017, ApJ, 846, 51
Ludlow A. D., Navarro J. F., Li M., Angulo R. E., Boylan-Kolchin M., Bett P. E., 2012, MNRAS, 427, 1322
Macciò A. V., Dutton A. A., van den Bosch F. C., Moore B., Potter D., Stadel J., 2007, MNRAS, 378, 55
Mantz A., Allen S. W., Rapetti D., Ebeling H., 2010, MNRAS, 406, 1759
Mantz A. B., Allen S. W., Morris R. G., Schmidt R. W., von der Linden A., Urban O., 2015, MNRAS, 449, 199
Maughan B. J., Jones C., Forman W., Van Speybroeck L., 2008, ApJS, 174, 117
Mayet F. et al., 2017, preprint (arXiv:1709.01255)
McCarthy I. G., Babul A., Holder G. P., Balogh M. L., 2003, ApJ, 591, 515
Meneghetti M., Rasia E., Merten J., Bellagamba F., Ettori S., Mazzotta P., Dolag K., Marri S., 2010, A&A, 514, A93
Meneghetti M. et al., 2014, ApJ, 797, 34
Mohr J. J., Fabricant D. G., Geller M. J., 1993, ApJ, 413, 492
Monaghan J. J., Lattanzio J. C., 1985, A&A, 149, 135
Monfardini A. et al., 2010, A&A, 521, A29
Motl P. M., Hallman E. J., Burns J. O., Norman M. L., 2005, ApJ, 623, L63
Nagai D., Vikhlinin A., Kravtsov A. V., 2007, ApJ, 655, 98
Neto A. F. et al., 2007, MNRAS, 381, 1450
Nurgaliev D. et al., 2017, ApJ, 841, 5
O'Hara T. B., Mohr J. J., Bialek J. J., Evrard A. E., 2006, ApJ, 639, 64
Okabe N., Zhang Y.-Y., Finoguenov A., Takada M., Smith G. P., Umetsu K., Futamase T., 2010, ApJ, 721, 875
Patel P., Maddox S., Pearce F. R., Aragón-Salamanca A., Conway E., 2006, MNRAS, 370, 851
Piffaretti R., Valdarnini R., 2008, A&A, 491, 71
Pinkney J., Roettiger K., Burns J. O., Bird C. M., 1996, ApJS, 104, 1
Planck Collaboration I, 2011, A&A, 536, A1
Planck Collaboration V, 2013, A&A, 550, A131
Planck Collaboration XXIX, 2014, A&A, 571, A29
Planck Collaboration XXVII, 2016, A&A, 594, A27
Plionis M., 2002, ApJ, 572, L67
Poole G. B., Fardal M. A., Babul A., McCarthy I. G., Quinn T., Wadsley J., 2006, MNRAS, 373, 881
Poole G. B., Babul A., McCarthy I. G., Fardal M. A., Bildfell C. J., Quinn T., Mahdavi A., 2007, MNRAS, 380, 437

Postman M. et al., 2012, ApJS, 199, 25
Prada F., Klypin A. A., Cuesta A. J., Betancort-Rijo J. E., Primack J., 2012, MNRAS, 423, 3018
Prokhorov D. A., Colafrancesco S., Akahori T., Million E. T., Nagataki S., Yoshikawa K., 2011, MNRAS, 416, 302
Rasia E. et al., 2006, MNRAS, 369, 2013
Rasia E., Mazzotta P., Bourdin H., Borgani S., Tornatore L., Ettori S., Dolag K., Moscardini L., 2008, ApJ, 674, 728
Rasia E. et al., 2012, New J. Phys., 14, 055018
Rasia E., Meneghetti M., Ettori S., 2013, Astron. Rev., 8, 40
Richstone D., Loeb A., Turner E. L., 1992, ApJ, 393, 477
Rizza E., Burns J. O., Ledlow M. J., Owen F. N., Voges W., Bliton M., 1998, MNRAS, 301, 328
Roncarelli M., Ettori S., Borgani S., Dolag K., Fabjan D., Moscardini L., 2013, MNRAS, 432, 3030
Rossetti M. et al., 2016, MNRAS, 457, 4515
Rumsey C. et al., 2016, MNRAS, 460, 569
Ruppin F. et al., 2017, preprint (arXiv:1712.09587)
Santos J. S., Rosati P., Tozzi P., Böhringer H., Ettori S., Bignamini A., 2008, A&A, 483, 35
Sayers J. et al., 2010, Proc. SPIE, 7741, 77410W
Schade D., Lilly S. J., Crampton D., Hammer F., Le Fevre O., Tresse L., 1995, ApJ, 451, L1
Sembolini F., Yepes G., De Petris M., Gottlöber S., Lamagna L., Comis B., 2013, MNRAS, 429, 323
Sembolini F., De Petris M., Yepes G., Foschi E., Lamagna L., Gottlöber S., 2014, MNRAS, 440, 3520
Shaw L. D., Holder G. P., Bode P., 2008, ApJ, 686, 206
Skibba R. A., Macciò A. V., 2011, MNRAS, 416, 2388
Slezak E., Durret F., Gerbal D., 1994, AJ, 108, 1996
Staniszewski Z. et al., 2009, ApJ, 701, 32
Sunyaev R. A., Zeldovich Y. B., 1970, Ap&SS, 7, 3
Sunyaev R. A., Zeldovich Y. B., 1972, Comments Astrophys. Space Sci., 4, 173
Swetz D. S. et al., 2011, ApJS, 194, 41
Ulmer M. P., Cruddace R. G., 1982, ApJ, 258, 434
Ventimiglia D. A., Voit G. M., Donahue M., Ameglio S., 2008, ApJ, 685, 118
Weißmann A., Böhringer H., Šuhada R., Ameglio S., 2013, A&A, 549, A19
Wen Z. L., Han J. L., 2013, MNRAS, 436, 275
Young A. et al., 2012, American Astron. Soc. Meeting Abstr., 219, 446.08
Zhang Y.-Y. et al., 2010, ApJ, 711, 1033

This paper has been typeset from a TEX/LATEX file prepared by the author.